

overall performance by the addition of small amounts of base to reduce proton diffusion into unexposed regions. We can estimate the width of the etched voxel to be  $\sim 1.0 \mu\text{m}$ . As the width of the voxel is much larger than that of the focal spot, the experimental conditions used to process the resist may not be optimized for achieving the smallest voxel. We are currently exploring other exposure and development conditions and modified resin systems to further improve the resolution in this type of 3D microlithography.

In conclusion, we have developed a chemically-amplified positive resist material and processing conditions that enable the microfabrication of buried 3D structures using two-photon lithography. The ability to selectively remove material in exposed regions allows for efficient creation of small hollow features within a larger solid body. By tailoring the polymer structure, it should be possible to fabricate the 3D structures with selected surface properties. For example, in our material, the pendent chemical groups at the patterned surface are methacrylic acid groups that provide a variety of options for surface functionalization. This feature may be useful for microfluidic devices for biological applications, and makes possible the study of both chemical and geometrical factors for such applications. These results suggest that positive tone two-photon 3D microfabrication may be a valuable route to precision microfluidic and micro-optical devices.

## Experimental

The polymers used in this study were synthesized by copolymerization of THPMA, MMA, and tBMA [18,19]. The number average molecular weight ( $M_n$ ) and the polydispersity of the copolymers were determined by gel permeation chromatography (THF, solvent) using polystyrene as the standard. The copolymer compositions were verified by  $^1\text{H}$  NMR measurements that were carried out in  $\text{CDCl}_3$  at room temperature with a Varian INOVA-400 spectrometer operating at 400 MHz for protons (Table 1). A two-photon 3D microfabrication resin system was created by blending 4 wt.-% of the two-photon acid generator [17] into the above-synthesized copolymers. 3D microfabrication was carried out using thick polymeric films ( $\sim 50 \mu\text{m}$ ) prepared by blade casting from  $\gamma$ -butyrolactone (GBL). The films were baked at  $90^\circ\text{C}$  for 1 h under a nitrogen atmosphere. The system for two-photon 3D microfabrication has been described elsewhere [17]. The PAG was excited with  $\sim 100$  fs pulses at a wavelength of 745 nm. The samples were mounted on a computer-controlled 3D translation stage. The incident beam was focused through an oil-immersion objective with a numerical aperture of 1.4. By scanning the focal point of the laser beam through the film, 2D and 3D patterns were defined. The total exposure dose is determined by the laser power and linear scan speed (dwell time in a voxel) of the stage. After exposure, the film was baked and developed in 0.26 N tetramethyl ammonium hydroxide (TMAH) aqueous solution and monitored by optical microscopy. The 3D microstructures shown in Figures 3 and 4 were fabricated by two-photon-exposure in a  $50 \mu\text{m}$  thick film of PMMA-THPMA (60:40). The patterns were exposed at 745 nm at an average power of  $40 \mu\text{W}$  and a linear scan speed of  $50 \mu\text{m s}^{-1}$ . After exposure, the film was baked for 1 min at  $90^\circ\text{C}$ . The target structure was then obtained by dissolving the exposed resin in aqueous 0.26 N tetramethyl ammonium hydroxide.

Received: August 19, 2002  
Final version: December 1, 2002

- [1] W. Denk, *Proc. Natl. Acad. Sci. USA* **1994**, *91*, 6629.
- [2] W. Denk, J. H. Strickler, W. W. Webb, *Science* **1990**, *248*, 73.
- [3] J. H. Strickler, W. W. Webb, *Opt. Lett.* **1991**, *16*, 1780.
- [4] J. H. Strickler, W. W. Webb, *Proc. Soc. Photo-Opt. Instrum. Eng.* **1990**, *1398*, 107.
- [5] E. S. Wu, J. H. Strickler, W. R. Harrell, W. W. Webb, *Proc. Soc. Photo-Opt. Instrum. Eng.* **1992**, *1674*, 776.

- [6] S. Maruo, O. Nakamura, S. Kawata, *Opt. Lett.* **1997**, *22*, 132.
- [7] S. Maruo, S. Kawata, *J. Microelectromech. Syst.* **1998**, *7*, 411.
- [8] D. A. Parthenopoulos, P. M. Rentzepis, *Science* **1989**, *245*, 843.
- [9] H. E. Pudavar, M. P. Joshi, P. N. Prasad, B. A. Reinhardt, *Appl. Phys. Lett.* **1999**, *74*, 1338.
- [10] K. Ikuta, K. Hirowatari, T. Ogata, in *Proc. of IEEE Int. Workshop on Micro Electro Mechanical Systems*, IEEE, Piscataway, NJ **1994**, p. 1.
- [11] T. Takagi, N. Nakajima, in *Proc. of IEEE Int. Workshop on Micro Electro Mechanical Systems*, IEEE, Piscataway, NJ **1994**, p. 211.
- [12] M. Horiyama, H. B. Sun, M. Miwa, S. Matsuo, H. Misawa, *Jpn. J. Appl. Phys.* **1999**, *38*, L212.
- [13] S. Maruo, K. Ikuta, *Appl. Phys. Lett.* **2000**, *19*, 2656.
- [14] M. Albota, D. Beljonne, J.-L. Brédas, J. E. Ehrlich, J.-Y. Fu, A. A. Heikal, S. E. Hess, T. Kogej, M. D. Levin, S. R. Marder, D. McCord-Maughon, J. W. Perry, H. Röckel, M. Rumi, G. Subramanian, W. W. Webb, X.-L. Wu, C. Xu, *Science* **1998**, *281*, 1653.
- [15] M. Rumi, J. E. Ehrlich, A. A. Heikal, J. W. Perry, S. Barlow, Z. Hu, D. McCord-Maughon, T. C. Parker, H. Röckel, S. Thayumanavan, S. R. Marder, D. Beljonne, J.-L. Brédas, *J. Am. Chem. Soc.* **2000**, *122*, 9500.
- [16] B. H. Cumpston, S. P. Ananthavel, S. Barlow, D. L. Dyer, J. E. Ehrlich, L. L. Erskine, A. A. Heikal, S. M. Kuebler, I.-Y. S. Lee, D. McCord-Maughon, J. Qin, H. Röckel, M. Rumi, X. Wu, S. R. Marder, J. W. Perry, *Nature* **1999**, *398*, 51.
- [17] W. Zhou, S. M. Kuebler, K. L. Braun, T. Yu, C. K. Ober, J. W. Perry, S. R. Marder, *Science* **2002**, *296*, 1106.
- [18] K. Ogino, J. S. Chen, C. K. Ober, *Chem. Mater.* **1998**, *10*, 3833.
- [19] S. Yang, J. Wang, K. Ogino, S. Valiyaveetil, C. K. Ober, *Chem. Mater.* **2002**, *12*, 33.
- [20] K. Asakawa, T. Ushirogouchi, M. Nakase, *Proc. Soc. Photo-Opt. Instrum. Eng.* **1995**, *438*, 563.
- [21] R. H. Webb, *Rep. Prog. Phys.* **2000**, *59*, 427.
- [22] M. Born, E. Wolf, *Principles of Optics*, 6th ed., Pergamon, Oxford **1993**.
- [23] S. M. Kuebler, M. Rumi, T. Watanabe, K. Braun, B. H. Cumpston, A. A. Heikal, L. L. Erskine, S. Thayumanavan, S. Barlow, S. R. Marder, J. W. Perry, *J. Photopolym. Sci. Technol.* **2001**, *14*, 657.

## Novel Oxides for Cycled Hydrogen Production from Methane and Water Using a Temperature Swing

Zhenchuan Kang and Zhong Lin Wang\*

A hydrogen-powered energy system has been proposed as the future basis of a green energy economy. Production, storage, distribution, and application of hydrogen are the main challenges for a hydrogen-based technology.<sup>[1]</sup> More than 90 % of the hydrogen today is made thermochemically through a process called reforming,<sup>[2]</sup> in which hydrocarbons are reacted with steam or oxygen at high temperature, typically  $800\text{--}1700^\circ\text{C}$ . Besides water electrolysis, research has been carried out to explore other hydrogen-production methods at low energy cost,<sup>[3]</sup> such as the sunlight powered photoelectrochemical cell.<sup>[4]</sup> Direct oxidation of methane has been achieved using ceria-supported metal catalysts, such as Pt, Rh, Cu, and Ni.<sup>[5,6]</sup> Ceria is frequently used because of its high activity for hydrocarbon oxidation and high ionic conductivity.<sup>[7]</sup>

[\*] Prof. Z. L. Wang, Dr. Z. Kang<sup>[+]</sup>  
School of Materials Science and Engineering  
Georgia Institute of Technology  
Atlanta, GA 30332-0245 (USA)  
E-mail: zhong.wang@mse.gatech.edu

[+] Present address: Research Center for Functional Rare Earth Higher Oxides, Institute of Geomechanics, Beijing 100081, China.

Exploration of composites of ceria and another oxide exhibiting a good electronic conductivity has been proposed.<sup>[8]</sup>

Most of the current approaches are targeted at stimulating the reforming process using ceria-based catalysts in the one-step reaction of  $\text{CH}_4 + \text{H}_2\text{O} \rightarrow \text{CO} + 3\text{H}_2$ . A large effort has been devoted to decreasing the reaction temperature in order to lower the energy cost, eliminating deactivation of the catalyst due to carbon deposition on its surface (coke formation), and improving the reaction rate. In this paper, we report a group of iron-doped rare-earth higher oxides of Ce, Tb, and Pr, which are designed as the oxygen supplier and storage material during a novel two-step reaction process that is carried out separately during the oxidation of methane and the reduction of water by swinging the reaction temperature.<sup>[9]</sup> The reactions are a cycling process and the working temperature is significantly lower than that required for reforming.

To illustrate our design, we use  $\text{Fe}_x\text{Ce}_{1-x}\text{O}_{2-\delta}$  as an example of the principle of the two-step separated reactions, where  $x$  is the amount of Fe doping and  $\delta$  represents, if any, a minor oxygen deficiency. The first step in this reaction cycle is the oxidation of  $\text{CH}_4$  by using the lattice oxygen transferred from the oxide:



This step is the first half of the cycle and is referred to as an oxygen “exile” process for the oxide. In the second step of the reaction cycle, the oxygen lost by the oxide has to be recovered so that it is ready for the next cycle of reaction. Therefore, this second step is designed to absorb oxygen from water vapor and recover the oxide back to  $\text{Fe}_x\text{Ce}_{1-x}\text{O}_{2-\delta}$ :



This oxygen “inhale” process also produces  $\text{H}_2$ . The two steps are conducted separately and consecutively to form a cycle that can be carried out continuously. The temperatures required for the two steps are different, thus, a swing in temperature is designed to reduce the energy cost.

Figure 1A shows the first step of the reaction cycle for  $\text{Fe}_{0.1}\text{Ce}_{0.9}\text{O}_2$ . A small reading in output voltage at temperatures lower than  $580^\circ\text{C}$  is likely due to the release of the oxygen bound at the surface. An appreciable amount of oxygen starts to release from the oxide lattice at  $\approx 580^\circ\text{C}$ . A jump in the output voltage of the fuel cell at  $\approx 670^\circ\text{C}$  indicates a significant increase in the production of hydrogen. The voltage steadily increases until  $700^\circ\text{C}$ , and then remains fairly stable as the temperature increases further. The release of oxygen is not constant, which is likely due to the formation of a series of homologous oxide phases.<sup>[10]</sup> In the second step of the reaction cycle (Fig. 1B), the temperature is kept at  $375^\circ\text{C}$ . Oxygen is taken away from  $\text{H}_2\text{O}$  by the oxide, and hydrogen is detected by the fuel cell after a delay. This is possibly due to a slower diffusion of the hydrogen through the reaction chamber and the fuel cell membrane, as well as a switch in gases between the two steps. Such a delay results in a steady output

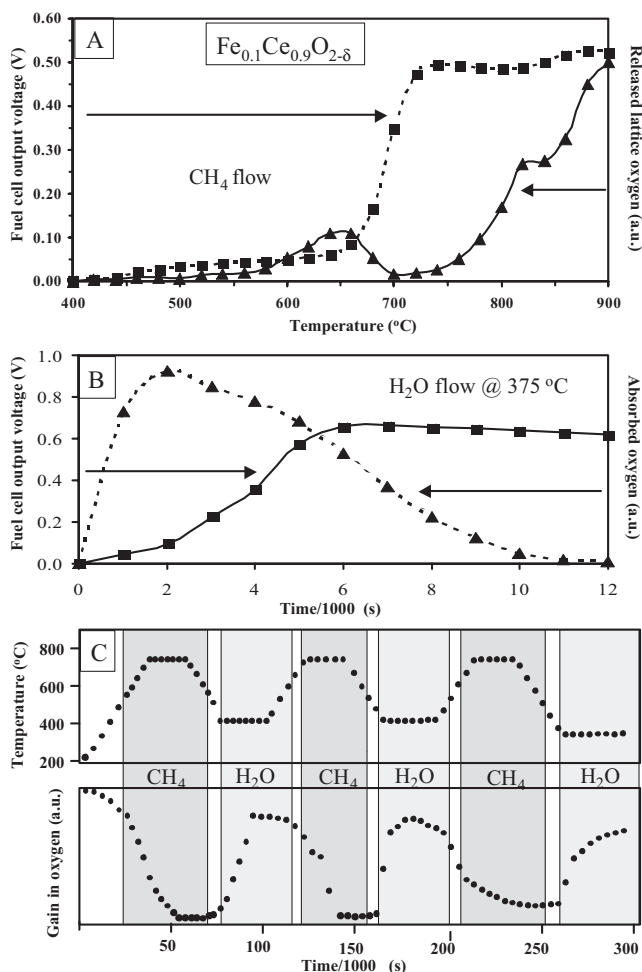


Fig. 1. The two-step reactions for hydrogen production from methane and water by the fluorite-type structured  $\text{Fe}_{0.1}\text{Ce}_{0.9}\text{O}_2$ . A) The output voltage of the fuel cell (squares), which is a quantitative measurement of the produced hydrogen, and the corresponding oxygen released from the oxide (triangles), measured by TGA as a function of the furnace temperature during the flow of methane. This reaction is the first half cycle of the process, during which hydrogen is produced through the oxidation of  $\text{CH}_4$  by lattice oxygen transferred from the oxide. B) Fuel cell output voltage (squares) and the absorbed oxygen from water vapor (triangles) at a constant temperature of  $375^\circ\text{C}$  as a function of time. This reaction is the second half cycle of the process, during which the lost oxygen in the oxide lattice is recovered from water vapor, resulting in hydrogen production as well. C) Three cycles of the temperature swing and the corresponding gain in oxygen of the oxide by alternatively flowing methane and water, showing the experimental feasibility of cycled production of hydrogen and a continuous usage of the oxide. Note the reduction temperature of water vapor was controlled to be  $375^\circ\text{C}$  for the first two cycles and  $315^\circ\text{C}$  for the third cycle, resulting in a slower oxygen gain in the third cycle.

voltage even after the absorption of oxygen is almost terminated at  $t = 10000$  s. The oxide now is fully oxygenated and is ready to start the next cycle. Shown in Figure 1C is the temperature swing and oxygen gain data for three consecutive cycles of the reactions. As the temperature is swung between  $750$  and  $375^\circ\text{C}$ , the loss and gain in oxygen are periodic as the incoming gases are switched between  $\text{CH}_4$  and  $\text{H}_2\text{O}$ , respectively, showing the experimental feasibility of cycled production of hydrogen without replacing the oxide.

For  $\text{Fe}_{0.1}\text{Tb}_{0.9}\text{O}_2$  (Fig. 2A), the lattice oxygen starts to be released at  $400^\circ\text{C}$ . A 40 s delay in hydrogen production until

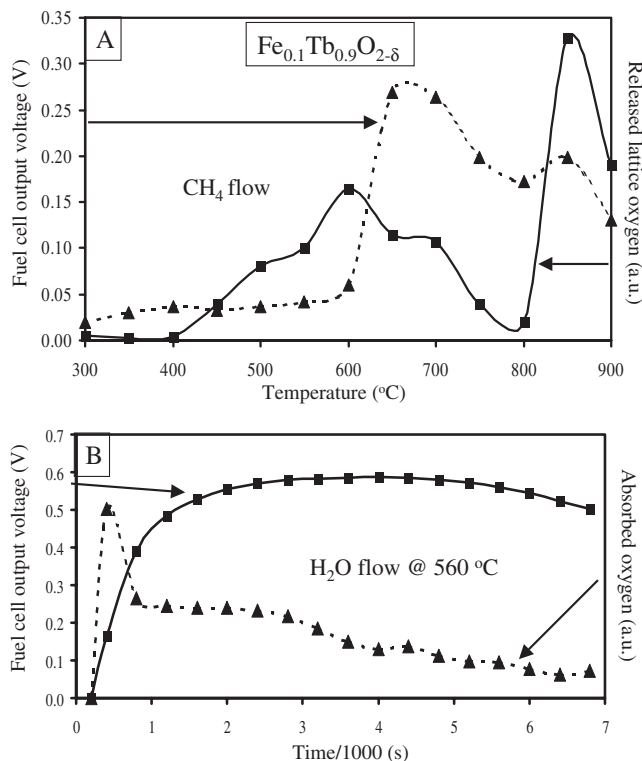


Fig. 2. The two-step reactions for hydrogen production from methane and water by the fluorite-type structured  $\text{Fe}_{0.1}\text{Tb}_{0.9}\text{O}_{2-\delta}$ . A) The output voltage of the fuel cell (triangles) and the corresponding oxygen released from the oxide (squares) as a function of the furnace temperature during the flow of methane. B) Fuel cell output voltage (squares) and the absorbed oxygen from water vapor (triangles) at a constant temperature of  $560\text{ }^\circ\text{C}$  as a function of time, showing a continuous release of hydrogen. The data prove the hydrogen production using fluorite-type structured terbium oxide through the two-step reaction process.

$600\text{ }^\circ\text{C}$  is due to the diffusion of the oxygen. In the second step, carried out at  $560\text{ }^\circ\text{C}$  (Fig. 2B), the absorbed oxygen experiences a jump in the first few hundred seconds, after which it decays steadily. The output voltage remains stable and constant, indicating a constant production of hydrogen.

For  $\text{Fe}_{0.1}\text{Pr}_{0.9}\text{O}_2$  (Fig. 3A), a pulsed release of oxygen at  $\approx 350\text{ }^\circ\text{C}$  results in an abrupt response in the fuel cell output voltage, which then remains fairly steady, indicating a stable production of hydrogen. The complex behavior of oxygen release depends on a number of factors, such as the possible homologous phases of the oxides, the partial oxygen pressure, the heating rate, and the characteristics of the cations. In the second step, i.e., reaction with  $\text{H}_2\text{O}$  at  $665\text{ }^\circ\text{C}$ , the production of hydrogen is stable and steady (Fig. 3B).

The three families of oxides presented above demonstrate that these oxides serve as an oxygen “pump” and have large oxygen transfer capacity. The doping of iron in the Ce, Tb, and Pr higher oxides is the key element to reduce the temperature required for the reduction in the second step of the reaction cycle. For  $\text{Fe}_{0.1}\text{Ce}_{0.9}\text{O}_2$ , for instance, the reduction temperature is reduced from  $550\text{ }^\circ\text{C}$  (for  $\text{CeO}_2$ )<sup>[11]</sup> to  $375\text{ }^\circ\text{C}$ . This is due to the larger electronegativity of 1.83 of Fe compared to that of 1.12 for Ce,<sup>[12]</sup> resulting in a lower temperature required for the reduction of  $\text{H}_2\text{O}$ . On the other hand, one still

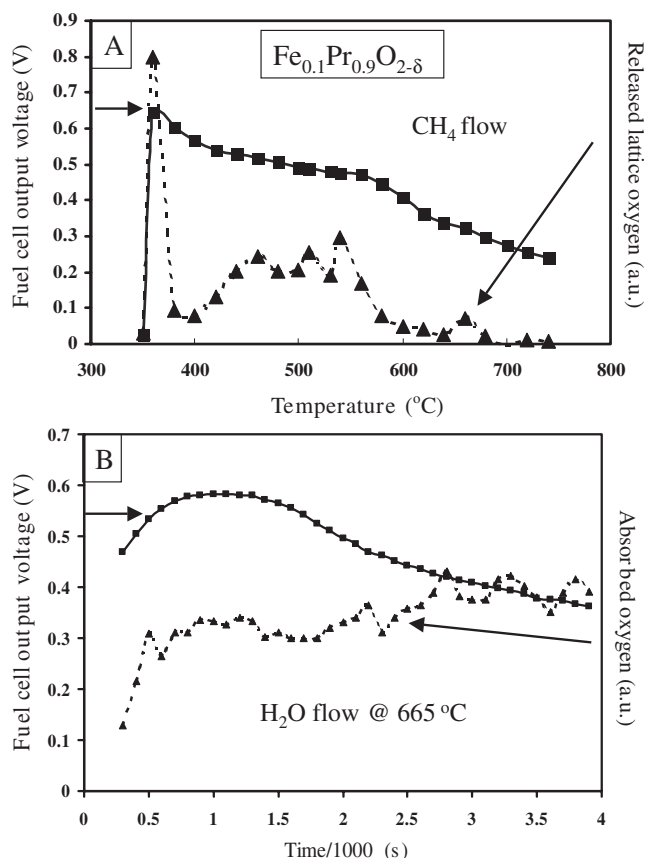


Fig. 3. The two-step reactions for hydrogen production from methane and water by the fluorite-type structured  $\text{Fe}_{0.1}\text{Pr}_{0.9}\text{O}_2$ . A) The output voltage of the fuel cell (squares) and the corresponding oxygen released from the oxide (triangles) as a function of the furnace temperature during the flow of methane. B) Fuel cell output voltage (squares) and the absorbed oxygen from water vapor (triangles) at a constant temperature of  $665\text{ }^\circ\text{C}$  as a function of time, showing a continuous production of hydrogen. The data prove the feasibility of hydrogen production using fluorite-type structured praseodymium oxide through the two-step reaction process.

cannot underestimate the catalytic effect of ceria due to its high activity for hydrocarbon oxidation.<sup>[7]</sup> To further elaborate this point and make a comparison, Figure 4 shows the two-step reactions for  $\text{Fe}_2\text{O}_3$ . The oxidation of  $\text{CH}_4$  is not appreciable until  $T > 775\text{ }^\circ\text{C}$ , and the reduction of water vapor requires a temperature as high as  $\approx 773\text{ }^\circ\text{C}$ . From a summary of the swing temperatures for the oxides presented above (Table 1), it is apparent that the operation temperatures for  $\text{Fe}_2\text{O}_3$  are the highest, which means that the reaction temperature cannot be lowered by solely using iron oxide. Doping the oxides of the rare-earth elements Ce, Pr, and Tb is likely the optimum approach, in which the catalytic property of the oxides is fully utilized. The swing temperatures for  $\text{Fe}_{0.1}\text{Ce}_{0.9}\text{O}_2$  are  $700$  and  $375\text{ }^\circ\text{C}$ , in contrast to  $350$  and  $665\text{ }^\circ\text{C}$  for  $\text{Fe}_{0.1}\text{Pr}_{0.9}\text{O}_2$ . The two reaction temperatures for  $\text{Fe}_{0.1}\text{Tb}_{0.9}\text{O}_2$  are very close, suggesting that no temperature swing may be needed for Tb based oxides. A temperature swing is cost effective for reducing the power consumption.

Platinum and nickel particles supported by ceria have been used in many reported experiments to accelerate the reaction

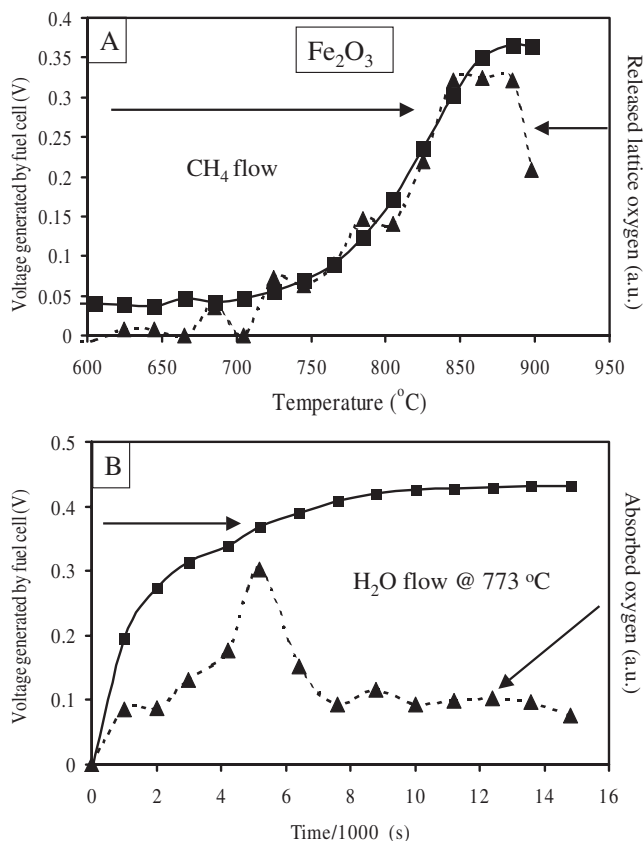


Fig. 4. The two-step reactions for hydrogen production from methane and water by Fe<sub>2</sub>O<sub>3</sub>. A) The output voltage of the fuel cell (squares) and the corresponding oxygen released from the oxide (triangles) as a function of the furnace temperature during the flow of methane. B) Fuel cell output voltage (squares) and the absorbed oxygen from water vapor (triangles) at a constant temperature of 773 °C as a function of time, showing a continuous release of hydrogen. The data show the possibility of hydrogen production using Fe<sub>2</sub>O<sub>3</sub> except the operation temperature is high.

Table 1. Swing temperatures for producing hydrogen through oxidation of methane and reduction of water vapor by the cycling two-step reactions.

Oxide	Oxidation of CH <sub>4</sub>	Reduction of H <sub>2</sub> O
Fe <sub>0.1</sub> Ce <sub>0.9</sub> O <sub>2</sub>	700 °C	375 °C
Fe <sub>0.1</sub> Tb <sub>0.9</sub> O <sub>2</sub>	600 °C	560 °C
Fe <sub>0.1</sub> Pr <sub>0.9</sub> O <sub>2</sub>	350 °C	665 °C
Fe <sub>2</sub> O <sub>3</sub>	800 °C	773 °C

rate of CH<sub>4</sub> oxidation. However, carbon deposition onto the catalytic surface results in coke formation, which is due to a decomposition of the synthesis gas at high temperature:



Carbon deposition may occur in the first step of the reaction cycle due to the higher reaction temperature. To assess the coke problem, structure analysis of Fe<sub>0.1</sub>Ce<sub>0.9</sub>O<sub>2-δ</sub> after three cycles of the two-step reactions is given in Figure 5.

High-resolution transmission electron microscopy (HRTEM) clearly shows that the surface is atomically clean without the presence of a thin amorphous carbon layer (Fig. 5A), indicating elimination of the deactivation problem. This means that the two-step reactions can be a continuous cycling process

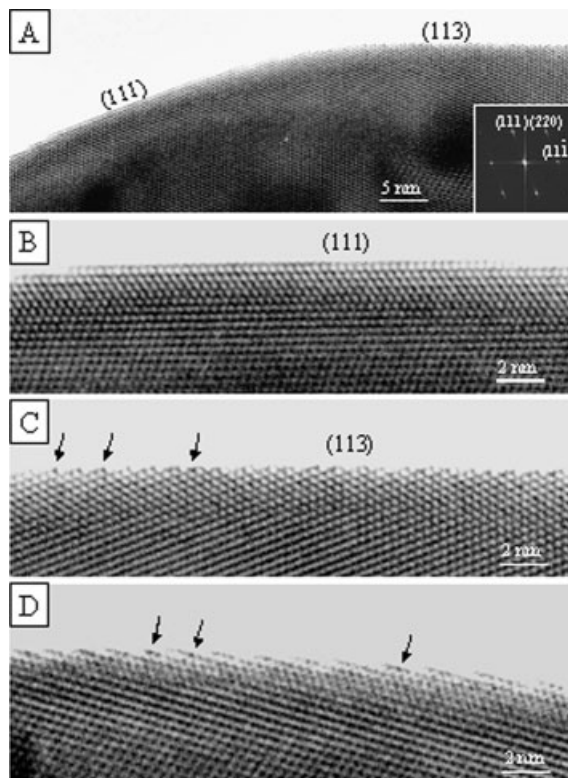
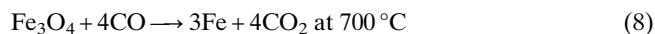
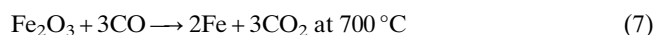
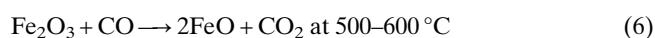
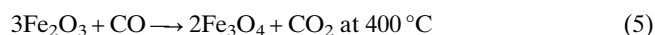


Fig. 5. High-resolution transmission electron microscopy study of the surfaces of Fe<sub>0.1</sub>Ce<sub>0.9</sub>O<sub>2</sub> after three cycles of the two-step reactions. The oxide powders were supported by a holey carbon film for TEM imaging. The surfaces of interest were imaged in profile, so that they are parallel to the direction of the incident electron beam. A) HRTEM profile image of the oxide surface, showing no residual carbon deposition on the surface. The inset is a Fourier transform of the image, from which the incident beam direction is identified to be [110]. B) A clean (111) surface of the oxide, displaying a perfectly ordered CeO<sub>2</sub> structure. The image contrast is periodic and ordered. C,D) HRTEM profile images of the (113) and a higher index surface of the oxide, showing some dark spots in contrast at the surfaces, as indicated by arrows. These spots are not periodic and they likely correspond to the segregation of Fe–O species at the surface. The Fe atoms are coordinated by oxygen atoms, but the 0.17 nm resolution of the HRTEM is not sufficient to resolve oxygen.

that can be carried out over and over again without replacing the oxide.

To understand the increased surface activity by iron doping, the surfaces of the oxides were studied by HRTEM. From the structural point of view, substitution of Ce by Fe may occur randomly in the cation sublattice throughout the volume, but HRTEM reveals some evidence for the presence of Fe atoms near the oxide surface. Shown in Figure 5B is a profile HRTEM image of the Fe<sub>0.1</sub>Ce<sub>0.9</sub>O<sub>2</sub> (111) surface, showing atomic flatness with little fluctuation in contrast. The large flat area results from the lower energy nature of the {111}, around which the perfect CeO<sub>2</sub> structure is preserved as judged by the image contrast and symmetry. The (113) surface displayed

in Figure 5C shows some dark contrast spots at the top layer, as indicated by the arrows, which likely correspond to the presence of the Fe–O species at the surface. The HRTEM image was recorded under the Schertzer defocus condition, so that the atoms appear in dark contrast when the sample is thin. The higher index surface shown in Figure 5D also shows some dark spots at the surface, which also support the claim of partial segregation of the Fe–O groups at the surface kinks and ledges. Since Fe is more active than Ce in reacting with water molecules,  $\text{Fe}_{0.1}\text{Ce}_{0.9}\text{O}_2$  preserves not only the high activity for hydrocarbon oxidation and high ionic conductivity as for native  $\text{CeO}_2$ ,<sup>[7]</sup> but also the high surface activity in reducing  $\text{H}_2\text{O}$  due to the presence of the Fe–O species. Therefore, the temperature needed for the step-two reaction is decreased. The Fe–O species on the surface could also minimize the coke problem and oxidize CO into  $\text{CO}_2$ <sup>[13]</sup> at relatively low temperature through the following reactions:



In the first step of the reaction cycle oxygen is released from the volume of the oxide with the formation of ordered superlattice structures,<sup>[14]</sup> but in the second step the surface activity is likely to be more important.

The fluorite-type structure of the oxides is based on the fundamental  $\text{CaF}_2$  unit, in which the cation has a face-centered-cubic (fcc) lattice, while the oxygen forms a cube case encapsulated inside the fcc lattice. This typical structure has a unique advantage of creating a high percentage of oxygen vacancies without a reconstructional phase transition in the cation sublattice<sup>[14]</sup> up to temperatures even higher than  $1000^\circ\text{C}$ , which is fundamental to the large oxygen transferring capacity of the oxides.<sup>[10]</sup> The oxygen sublattice is independent and the migration of an oxygen ion does not require a substantial cooperative movement of any cation, because the valence variation of the Ce, Pr, and Tb ions between valence 4+ and 3+ can easily accommodate oxygen vacancies. The isothermal<sup>[15–17]</sup> and isobaric<sup>[18–20]</sup> data for  $\text{RO}_{2-x}$  (R = Ce, Tb, Pr) are available.  $\text{RO}_2$  can be reduced reversibly to  $\text{RO}_{1.714}$ ,<sup>[14]</sup> releasing a large amount of oxygen. Therefore, the oxides are non-smashable during the reactions and temperature swing, thus eliminating cracking and fracture problems.

In summary, we have presented a series of iron-doped oxides of Ce, Tb, and Pr that have been used to produce hydrogen in a two-step reaction process by separately oxidizing methane and reducing water vapor via a temperature swing. Iron-doped ceria, for example, lowers the reduction

temperature of water vapor from  $550$  to  $375^\circ\text{C}$ , due to stimulated surface activity by segregated Fe–O groups at the surface, with the potential of improving the efficiency of hydrogen production. Besides the catalytic effect, the oxide also directly participates in the reactions by releasing oxygen out of the lattice and re-absorbing oxygen into the lattice without a reconstructional phase transition. The oxide has overcome the catalyst deactivation problem by removing the surface-coated carbon via oxidation. Therefore, the cycle can be carried out continuously without replacing the oxide by switching between methane and water vapor accompanied by a temperature swing. The oxide materials and method presented in this paper provide a new approach that is likely to produce hydrogen at low cost and high efficiency. Lowering the operation temperature introduces the potential of using sunlight thermoradiation for hydrogen production, leading to a new field of hydrogen research and application.

### Experimental

The oxide samples were prepared as follows: First, we prepared one mole each of cerium nitrate, praseodymium nitrate, and terbium nitrate solution, and one mole iron nitrate. Then  $90\text{ cm}^3$  cerium nitrate (praseodymium nitrate or terbium nitrate) solution was mixed with  $10\text{ cm}^3$  of iron nitrate solution in a beaker with vigorous stirring for 30 min. Then  $\text{NH}_4\text{OH}$  was added to the mixed solutions and the pH was adjusted to 8 with vigorous stirring. The precipitates were washed with deionized water at least 3–5 times, and then were dried at room temperature. This was followed by heating up to  $800^\circ\text{C}$  for 30 min in a furnace and cooling down to room temperature. The structures of the oxides were confirmed by X-ray diffraction, transmission electron microscopy, and energy dispersive X-ray spectroscopy. The microstructure of the oxides prior to and after the reactions was studied by high-resolution transmission electron microscopy (HRTEM) at 400 kV using a JEOL 4000EX.

To achieve the principle laid out by the two-step reactions in Eqs. 1 and 2, a gas-flow and reaction apparatus was constructed. For the first step of the reaction cycle, argon carrier gas containing 15% of  $\text{CH}_4$  was used for the reduction of the oxide. The oxide powder was loaded into a quartz container that was suspended on one arm of a Cahn thermobalance, which was enclosed by a large quartz chamber with gas inlet and outlet set up. A temperature-programmed furnace (Eurotherm) was raised to surround the quartz container. The exit gas was led through a fuel cell (Warsitz Enterprises, Inc.), consisting of a stack of proton exchange membranes. The voltage output of the fuel cell gave a quantitative measurement of the amount of produced  $\text{H}_2$ . The release/gain of oxygen from/to the oxide and the reduction of  $\text{CH}_4$  were monitored by detecting the weight loss/gain of the oxide by the Cahn thermobalance (e.g., thermogravimetric analysis, TGA). In the second step of the reaction, helium gas carrying water vapor was introduced into the reaction chamber, and the temperature was controlled to ensure a high production rate of  $\text{H}_2$ . Again, the amount of produced hydrogen was monitored by the output voltage of the fuel cell. In the entire two-step reaction process, the gas flow rate was  $10\text{--}30\text{ cm}^3\text{ min}^{-1}$ , the chamber pressure was 1 bar, and the heating and cooling rates were  $1^\circ\text{C min}^{-1}$ .

Received: November 13, 2002

- [1] J. M. Ogden, *Phys. Today* **2002**, April, 69.
- [2] K. Kochloeff, in *Handbook of Heterogeneous Catalysis*, Vol. 4 (Eds: G. Ertl, H. Knozinger, J. Wetkamp), Wiley-VCH, Weinheim **1997**, p. 1819.
- [3] *Proc. 2001 US DOE Hydrogen Program Review*, US Department of Energy, Washington DC **2002**. Available at <http://www.eren.doe.gov/hydrogen/docs/30535toc.html>
- [4] O. Khaaselev, J. A. Turner, *Science* **1998**, *280*, 425.
- [5] S. Park, J. M. Vohs, R. J. Gorte, *Nature* **2000**, *404*, 265.
- [6] D. A. Hickman, L. D. Schmidt, *Science* **1993**, *259*, 343.
- [7] A. Trovarellie, *Catal. Rev. Sci. Eng.* **1996**, *38*, 439.
- [8] B. C. H. Steele, *Nature* **2000**, *400*, 619.
- [9] Z. C. Kang, Z. L. Wang, *US Patent*, pending.
- [10] Ce, Pr, and Tb have valences of 3+ and 4+. They form mixed valent oxides that can be represented by a homologues series  $\text{R}_n\text{O}_{2n-2m}$ . (for a compre-

hensive review see Z. L. Wang, Z. C. Kang, *Functional and Smart Materials—Structural Evolution and Structure Analysis*, Plenum Press, New York **1998**, Ch. 4). These oxides were formed by introducing ordered oxygen vacancies in the fluorite-based unit, but the fcc cation sublattice is a superstable frame, which is independent of the distribution of oxygen vacancies.

- [11] K. Otsuka, Y. Wang, E. Sunada, I. Yamanaka, *J. Catal.* **1998**, *175*, 152.  
 [12] J. P. Schaffer, A. Saxena, S. D. Antolovich, T. H. Sanders, S. B. Warner, *The Science and Design of Engineering Materials*, 2nd ed., McGraw-Hill, New York **1997**, Appendix B.  
 [13] Oxidation of CO is usually carried out using a metal catalyst such as Pt, see D. C. Skelton, R. G. Tobin, D. K. Lambert, C. L. DiMaggio, G. B. Fisher, *J. Phys. Chem. B* **1999**, *103*, 946.  
 [14] Z. L. Wang, Z. C. Kang, *Functional and Smart Materials—Structural Evolution and Structure Analysis*, Plenum Press, New York **1998**, Ch. 4.  
 [15] R. E. Ferguson, E. D. Guth, L. Eyring, *J. Am. Chem. Soc.* **1954**, *76*, 3890.  
 [16] J. M. Honig, A. F. Clifford, P. A. Faeth, *Inorg. Chem.* **1963**, *2*, 791.  
 [17] R. G. Haore, L. Eyring, *Handb. Phys. Chem. Rare Earths* **1994**, *18*, 413.  
 [18] B. G. Hyde, D. J. M. Bevan, L. Eyring, *Philos. Trans. R. Soc. London, A* **1966**, *259*, 583.  
 [19] J. Kordis, L. Eyring, *J. Phys. Chem.* **1968**, *72*, 2030.  
 [20] J. Kordis, L. Eyring, *J. Phys. Chem.* **1968**, *72*, 2044.

## Quantum Confinement Observed in ZnO/ZnMgO Nanorod Heterostructures\*\*

By Won Il Park, Gyu-Chul Yi,\* Miyoung Kim, and Stephen J. Pennycook

One-dimensional nanostructures, including nanotubes, nanowires, and nanorods, are potentially ideal functional components for nanometer-scale electronics and optoelectronics.<sup>[1–3]</sup> Homogeneous carbon nanotubes and nanowires have already been employed in various nanoscale devices.<sup>[4–6]</sup> However, the ability to fabricate nanoscale heterostructures with well-defined crystalline interfaces opens up many new device applications, as already proven in thin-film semiconductor electronics and photonics.<sup>[7]</sup> In particular, embedding quantum structures in a single nanorod would enable novel physical properties such as quantum confinement to be exploited, for example, the continuous tuning of spectral wavelength by varying the well thickness. Here, we report the catalyst-free fabrication of quantum-well nanorod heterostructures that exhibit atomically abrupt interfaces and a well-width dependent blue shift resulting from quantum confinement. The ability to grow tun-

able quantum-well heterostructure nanorods is expected to greatly increase the versatility and power of these building blocks for applications in nanoscale photonics and electronics.

Quantum confinement effects in heterostructure nanowires or nanorods have not been clearly observed despite the recent synthesis of compositionally modulated nanowire superlattices by the vapor–liquid–solid (VLS) growth process.<sup>[8–10]</sup> This may result from the relatively broad heterostructure interfaces caused by re-alloying of alternating reactants in the metal catalyst during the condensation–precipitation process.<sup>[8]</sup> In that case, abrupt interfaces would be expected using a non-catalytic growth technique to minimize the formation of a mixed interfacial layer,<sup>[11]</sup> i.e., by utilizing direct adsorption of atoms on the top surface of nanorods. Nanoscale heterostructures can then be formed by direct epitaxial growth using the techniques already developed for growth of thin-film heterostructure devices. In this paper, we demonstrate this to be the case by the fabrication of quantum-well structures within individual nanorods. With precise thickness control down to the monolayer level, these heterostructures show the clear signature of quantum confinement, an increasing blue-shift with decreasing layer thickness, which is in good agreement with theoretical predictions.

Our approach to fabricating heterostructure nanorods utilizes metal–organic vapor phase epitaxy (MOVPE) to grow high-quality ZnO nanorods,<sup>[11]</sup> thus eliminating the metal catalyst usually required in other methods.<sup>[12]</sup> To fabricate heterostructures within the nanorods, Zn<sub>1–x</sub>Mg<sub>x</sub>O ( $x < 0.3$ ) alloy was employed since it has a lattice mismatch with ZnO of less than 1 % as well as a larger bandgap.<sup>[13]</sup> ZnO nanorods were first prepared on Al<sub>2</sub>O<sub>3</sub>(00-1) substrates using MOVPE.<sup>[11]</sup> Nanorods are formed as a result of preferential growth along the *c*-axis of ZnO, offering an ideal method for fabrication of nanoscale heterostructures. By introducing Mg precursor into the reactor, Zn<sub>1–x</sub>Mg<sub>x</sub>O layers were epitaxially grown only on the tips of the ZnO nanorods. This growth method ensures minimal intermixing, since no dissolution is required in a catalyst particle, and creates sharp interfaces that enable a wide family of structures and devices to be fabricated.

The multiple quantum well (MQW) nanorods prepared in this study consist of 10 periods of Zn<sub>0.8</sub>Mg<sub>0.2</sub>O/ZnO on ZnO nanorods (a schematic diagram of the MQW nanorods is shown in Fig. 1A). For ZnO nanorod growth, we employed diethylzinc (DEZn) and oxygen as the reactants with argon as the carrier gas. Details of the ZnO nanorod growth are described elsewhere.<sup>[11]</sup> For Zn<sub>1–x</sub>Mg<sub>x</sub>O growth bis(cyclopentadienyl)magnesium (Cp<sub>2</sub>Mg) was used as the Mg precursor, with composition controlled through the partial pressure.<sup>[13]</sup> The growth time for the ZnMgO barrier layers was fixed at 36 s, while growth times for the ZnO well layers were set at 12, 18, and 27 s, resulting in well widths of 1.1, 1.7, and 2.5 nm, respectively, as determined by transmission electron microscopy (TEM). The compositions of the Zn<sub>1–x</sub>Mg<sub>x</sub>O layers in the heterostructure and MQW nanorods were determined by energy dispersive X-ray spectroscopy and for all samples  $x$  was approximately 0.2.

[\*] Prof. G.-C. Yi, W. I. Park  
 Department of Materials Science and Engineering  
 Pohang University of Science and Technology (POSTECH)  
 Pohang, Kyungbuk 790-784 (Korea)  
 E-mail: gcyi@postech.ac.kr  
 Dr. M. Y. Kim  
 Samsung Advanced Institute of Science and Technology  
 PO Box 111, Suwon 440-600 (Korea)  
 Dr. S. J. Pennycook  
 Oak Ridge National Laboratory  
 PO Box 2008, Oak Ridge, TN 37831-6030 (USA)

[\*\*] This research was supported by the National Program for Nanostructured Materials Technology of the Ministry of Science and Technology as one of the 21st century Frontier Programs and in part by the Division of Materials Sciences, U.S. Department of Energy, under contract DE-AC05-00OR22725 with Oak Ridge National Laboratory managed by UT-Battelle, LLC. Extensive use of the facilities at POSTECH is acknowledged.